

Dynamic characterization and FE model updating via metaheuristic algorithm of two confined masonry buildings

Original

Dynamic characterization and FE model updating via metaheuristic algorithm of two confined masonry buildings / Cucuzza, R.; Civera, M.; Aloisio, A.; Ricciardi, G.; Domaneschi, M.. - In: ENGINEERING STRUCTURES. - ISSN 0141-0296. - 308:(2024), pp. 1-15. [10.1016/j.engstruct.2024.117935]

Availability:

This version is available at: 11583/2987795 since: 2024-04-14T07:36:14Z

Publisher:

Elsevier

Published

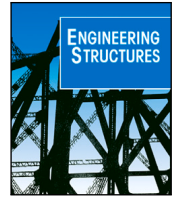
DOI:10.1016/j.engstruct.2024.117935

Terms of use:

This article is made available under terms and conditions as specified in the corresponding bibliographic description in the repository

Publisher copyright

(Article begins on next page)



Dynamic characterization and FE model updating via metaheuristic algorithm of two confined masonry buildings

Raffaele Cucuzza^a, Marco Civera^a, Angelo Aloisio^b, Giuseppe Ricciardi^c, Marco Domaneschi^{a,*}

^a Department of Structural, Geotechnical and Building Engineering, Politecnico di Torino, Turin, Italy

^b Department of Civil, Construction-Architectural and Environmental Engineering, Università degli Studi dell'Aquila, L'Aquila, Italy

^c Department of Engineering, University of Messina, Messina, Italy

ARTICLE INFO

Keywords:

Confined masonry
Ambient vibration tests
FE model updating
Optimization
Seismic vulnerability

ABSTRACT

This paper investigates the dynamic characteristics and Finite element model updating of two confined masonry buildings in Messina, constructed in the aftermath of the devastating 1908 earthquake. The study addresses the need for advanced research in this field to enhance the understanding of the dynamic behaviour of confined masonry structures. The authors identified the modal parameters of the buildings from ambient vibration tests. Finite element models have been developed and fine-tuned in a second step to optimize the agreement between the simulated and observed modal parameters. The optimized parameters are then compared with the outcomes of nondestructive tests on masonry and reinforced concrete. This research addresses the modelling issues when dealing with confined masonry structures, offering guidance to engineers to select the modelling parameters. The paper emphasizes the substantial stiffening effect introduced by confined masonry, as evidenced by the optimized Young's modulus of masonry, which is almost two and a half times higher than values obtained from flat jack tests. To accurately represent the interaction between reinforced concrete ties and masonry panels within equivalent frame models, it becomes crucial to adequately overstate the masonry stiffness to capture the mutual coupling between structural components.

1. Introduction

Confined masonry (CM) with reinforced concrete (RC) is a construction technique used to enhance earthquake resistance and structural integrity of unreinforced masonry (URM). It combines two building materials: masonry and reinforced concrete; see Fig. 1. The primary load-bearing elements are masonry walls, typically built using bricks, concrete blocks, or stone. Horizontal and vertical bands or reinforced concrete belts are integrated into the structure [1].

The tie elements confine the masonry walls, enhancing their deformation capacity and connectivity with adjacent walls and floor diaphragms. Toothed edges or joint reinforcements can strengthen the bond between the masonry wall and the RC tie vertical confinement elements. This strategy effectively delays the onset of unwanted cracking and separation at the interface, even when subjected to repeated loads [2,3].

CM with RC is safer than traditional, unreinforced masonry construction in earthquake-prone regions. It reduces the vulnerability of the building and lowers the risk of casualties and property damage during earthquakes. CM has been employed globally, from simple,

unengineered single-storey homes to engineered multi-storey buildings. Moreover, it continues to undergo developments, gaining popularity as a construction method worldwide [1,4–6]. Incorporating distributed reinforcement or confining elements substantially enhances the seismic performance of unreinforced masonry. This improvement results in increased lateral resistance and ductility [7–9].

CM buildings have generally performed satisfactorily in past earthquakes [10]. Failure modes in CM structures typically involve shear-induced in-plane damage, such as bed joint sliding and diagonal shear cracking that originates at the centre of the masonry walls and extends towards the tie columns and/or vertical confinements. Recent seismic events have also highlighted several factors that increase the vulnerability of CM buildings, including poor site conditions, sub-par workmanship, weaker masonry materials, irregular construction practices, improper detailing, and non-compliance with construction guidelines [11,12]. In numerous instances, particularly in Latin American nations, there is a systematic lack of professional counselling during the design and construction of housing [13].

* Corresponding author.

E-mail addresses: raffaele.cucuzza@polito.it (R. Cucuzza), marco.civera@polito.it (M. Civera), angelo.aloisio1@univaq.it (A. Aloisio), giuseppe.ricciardi@unime.it (G. Ricciardi), marco.domaneschi@polito.it (M. Domaneschi).

<https://doi.org/10.1016/j.engstruct.2024.117935>

Received 30 September 2023; Received in revised form 4 March 2024; Accepted 24 March 2024

0141-0296/© 2024 The Author(s). Published by Elsevier Ltd. This is an open access article under the CC BY-NC-ND license (<http://creativecommons.org/licenses/by-nc-nd/4.0/>).

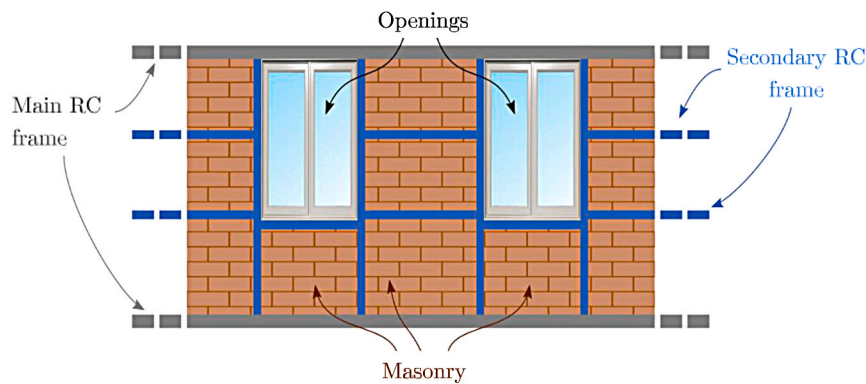


Fig. 1. Graphical representation of a Confined Masonry (CM) structure.

These damage reports reveal gaps in the analysis and design processes that must be addressed to ensure CM buildings' safe and cost-effective design. Ruiz et al. [14] highlighted the significance of uncertainty in CMB while developing fragility curves using an extensive experimental dataset. They observed significant variability between specimens and noted that the results were highly dependent on the brick type, the inclusion of horizontal steel reinforcements within the mortar joints, and the vertical compressive stress applied during testing. Additionally, Lovon et al. [15] also showed that the seismic safety of the informally built CMB is not generally code-conforming.

The CM system was introduced in Italy as an alternative to unreinforced masonry (URM) buildings after the 1908 earthquake in Messina. Messina experienced one of the most devastating earthquake events in modern history: the 1908 Messina earthquake, with a magnitude of 7.1 on the Richter scale. This earthquake, accompanied by a tsunami, resulted in over 100,000 fatalities and the destruction of approximately 91% of the structures in Messina.

Following the devastating earthquake, new seismic regulations were implemented in Italy. The R.D. n. 2089 (23/10/1924) [16] imposed restrictions on building heights and introduced guidelines for constructing earthquake-resistant structures. These guidelines encompassed the CM system, which became the most prevalent construction method during the post-1908 earthquake reconstruction. This approach continued to be widely adopted in construction practices until the outbreak of the Second World War.

In recent years, much of the research on CM has been centred on mechanical characterization, primarily through quasi-static and shake table tests, as well as the advancement of modelling approaches [17–23]. With well-established mechanical characterization findings, the focus has now shifted towards the development of innovative retrofitting solutions [24–26].

Only a handful of studies conducted ambient vibration tests (AVT) on CM structures. AVTs have predominantly been carried out on RC and steel buildings, with a minor focus on masonry structures [27–29]. Limited research papers delved into the dynamic identification of CM structures; see [30,31], who analyse CM buildings in India. Consequently, the experimental estimation of modal characteristics for CM buildings through AVT is still in its early stages of development [32].

Seismic vulnerability analysis necessitates the development of simplified finite element (FE) models that balance accuracy and complexity, as highlighted in [33]. Consequently, there is a need for research endeavours and case studies focused on confined masonry (CM) structures. Such studies serve a dual purpose. First, they investigate the predictive capabilities of simplified modelling approaches when estimating modal parameters. Secondly, they offer insights to engineers for selecting the optimal modelling parameters. It is worth noting that CM structures introduce significant uncertainties in material parameters, especially in historical buildings. Therefore, to gain a comprehensive

understanding of the seismic performance of CM structures under various loading scenarios, it is essential to investigate the dynamics of these buildings at low-level vibrations.

This study investigates the dynamic characteristics and Finite Element model updating of two CM buildings in Messina, built after the devastating 1908 earthquake. The authors conducted dynamic identification using an enhanced version of Stochastic Subspace Identification (SSI) based on the Montecarlo Stabilization diagram (MCSD), specifically, Phase 1 of the recently introduced Intelligent Automated Operational Modal Analysis (i-AOMA) method [34]. This approach mitigated the subjectivity of selecting input parameters in the SSI method. Subsequently, the authors fine-tune the FE models of these structures to derive estimates of the material parameters, aiming to achieve a close match between experimental and numerical modal parameters.

The paper's structure unfolds as follows: it starts with a brief introduction outlining the building characteristics and the outcomes of geometric and destructive tests performed on the structures. Subsequently, the authors present the results of dynamic identification utilizing the MCSD. The paper describes and optimizes the Finite Element models, as discussed in the last section.

2. Description of the masonry complex

This paper characterizes two buildings at the University of Messina. The first one houses the Department of Political and Legal Sciences (SCIPOG) and is located in Piazza XX Settembre, Messina, referred to as Complex No. 1. The second building, located in Via della Concezione, hosts Messina's Department of Cognitive, Psychological, Pedagogical, and Cultural Studies (COSPECS), called Complex No. 2.

Both buildings were constructed during the fascist period as part of the post-disaster recovery campaign "Servizio Terremoto", initiated by the Italian Government in response to the tragic 1908 earthquake. To be more specific, historical documents from that era indicate that the former building was erected in 1926, while the latter was completed in 1931, with each project being undertaken by separate construction companies.

Complex No. 1 in Piazza XX Settembre, shown in Fig. 2(a), is located on a variably shaped, flat plot of land bordered by public roads in all directions. The structure comprises three levels, including one basement and two above-ground floors. Two separate staircases provide access to the basement; a fourth level includes the staircase tower's roof. Internally, the building adjoins outdoor space, partly green and partly paved. The entire building covers an area of approximately 1000 m² on the basement and ground floors and about 800 m² on the first floor. The construction type of the building is RC CM.

Complex No. 2 in Via della Concezione (Fig. 2(b)) has one basement, one ground floor (which includes a mezzanine), a first floor, and a partly accessible roof. The basement can be accessed through two separate staircases, while the ground floor is reachable via a small



Fig. 2. Views of the two buildings: (a) Complex No. 1 in Piazza XX Settembre; and (b) Complex No. 2 in Via della Concezione.

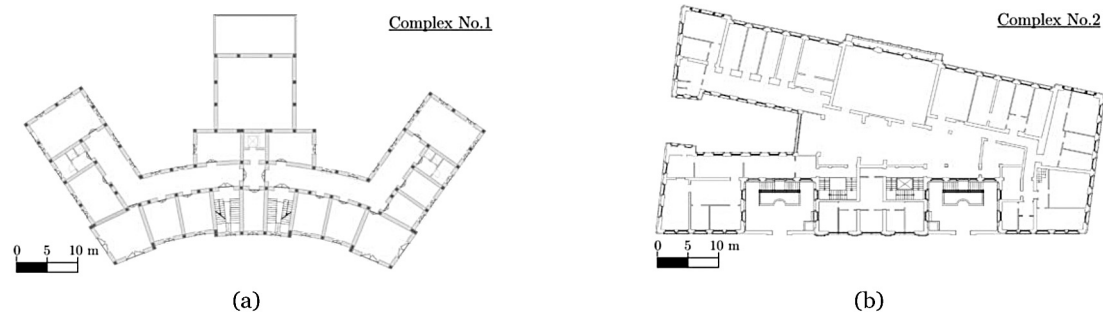


Fig. 3. Plans of the first floor of (a) Complex No. 1 and (b) Complex No. 2.

ramp in front of the main entrance on the public road. The building under study is situated on level ground and is bordered by public streets to the east, south, and west, while it shares its northern border with another privately owned building. Along the main facade of the building (Via Concezione), two small courtyards are present, each equipped with an external staircase providing access to the ground floor. The entire building covers a total indoor area of approximately 1370 m². Fig. 3(a),(b) show the plans of the first floor of Complex No. 1 and 2, respectively.

3. Geometric and mechanical characterization

The testing plan encompasses on-site and laboratory investigations comprising destructive, semi-destructive, and non-destructive methods. For the two complexes, the analyses included two endoscopic examinations for masonry characterization, 15 tests on reinforced concrete and/or masonry elements, 12 magnetometric surveys with a pacometer, 12 core samples taken from concrete with subsequent compression testing, six rebar extractions with tensile testing, two single-plate jacks for estimating in-situ stress within the investigated masonry section, two double-plate jacks for mechanical characterization (compressive strength) of the load-bearing masonry. The performed tests and the strategical position of the different types of survey have been conducted aiming to satisfy at least the minimum level of knowledge required by the Italian Standard regulation NTC2018 [35] for both the masonry and RC elements. With specific regard to the former, in chapter 10.10.1 of NTC2018, it is recommended at least one sample for 650 m³ of delivery when masonry belongs to Category I as in the specific case. Moreover, visual surveys must be conducted to evaluate the typology and quality of the masonry as well as the degree of amortization. On the other hand, surveys on the RC elements have been conducted according to the recommendations provided by chapter 8.5.4.2 of NTC2018, in which at least one concrete specimen and one steel reinforcement sample must be picked up for 300 m² of covered surface.

In all instances, the endoscopic examinations revealed an average of 2 cm plaster and solid brick masonry with mortar joints. The bricks composing the external and internal masonry of the ground floor do have dimensions of approximately 8 cm × 30 cm × 20 cm while 12 cm × 24 cm × 6 cm for the masonry belonging to the first floor. The columns vary in size, ranging from 60 cm to 12 cm in width, accompanied by longitudinal reinforcements ranging from $\Phi 30$ to $\Phi 12$. Stirrups span a range from 20 cm to 10 cm in length. The floor structures consist of 20 cm RC solid slabs supported by RC beams.

Fig. 4(a) illustrates a detailed view of the CM masonry, showing an RC vertical confinement element adjacent to solid brick masonry. In Fig. 4(b), the reinforcement of a 12 cm vertical confinement can be observed. As previously mentioned, the flooring comprises a solid RC slab, with intrados plastering supported by a reed, as depicted in Fig. 4(c)–(d).

The masonry generally appears homogeneous, as indicated by thermal analysis conducted throughout the entire structure, as proven by Fig. 5.

Table 1 presents the results of compression tests conducted on concrete samples. Complex No. 1's mean compressive strength is approximately 12.33 MPa, indicating moderate compressive strength. Such values are commonly found in historical RC structures. The standard deviation for Complex No. 1 is around 1.98 MPa, corresponding to a low coefficient of variation (16%). This low variation is a positive indication of consistent concrete quality within this complex. In the case of Complex No. 2, the mean compressive strength is similar to that of Complex No. 1, at approximately 11.92 MPa, with a slightly higher standard deviation of 2.98 MPa. The increased variability in Complex No. 2's concrete strength suggests that some samples may exhibit significantly lower strength values. This variability could be attributed to differences in the concrete mix or curing conditions during construction.

Table 2 provides an overview of the results from tensile tests conducted on steel samples. For Complex No. 1, the average yielding



Fig. 4. (a) View of the CM structure and (b) a typical vertical RC element. (c)–(d) show the intrados floor.



Fig. 5. Thermal analysis of the CM.

strength (f_y) is approximately 287.53 MPa, and the ultimate strength (f_u) is nearly 409.93 MPa. The steel rebars exhibit satisfactory strength, making them suitable for structural applications. The standard deviation for f_y and f_u is relatively low, at 32.24 MPa and 51.48 MPa, respectively. This low variation suggests consistent quality in the steel materials used within this complex. Complex No. 2 displays similar trends in steel strength properties. The average yielding strength (f_y) is approximately 263.90 MPa, and the ultimate strength (f_u) is approximately 378.36 MPa. While these values are slightly lower than those of Complex No. 1, they still indicate good strength properties for structural elements. The standard deviations for f_y and f_u in Complex No. 2 are 34.05 MPa and 54.57 MPa, respectively, suggesting reasonable consistency in steel quality, although slightly more variability than Complex No. 1.

Table 3 summarizes the results from flat jack tests performed on the two complexes. The tests were conducted following the ASTM C1196-14a standards. Complex No. 1's compressive strength (σ_u) was 1.96 MPa. In contrast, Complex No. 2 exhibited a notably lower compressive strength of 0.87 MPa, revealing a potential structural difference between the two complexes. Consequently, the masonry in Complex No. 1 bears a static load equivalent to 4% of its capacity, while in Complex No. 2, the static stress is 15% the capacity. This difference can be primarily attributed to the lower compressive strength observed in Complex No. 2. Tests no. 2 are reported for completeness but do not

yield reliable results reasonably due to the inherent dis-homogeneity induced by the construction type. Further investigations and data collection are recommended to draw more consolidated outcomes due to the limited measurement points. However, the authors assessed the reliability of the experimental results obtained by the masonry by analysing the results of other experimental tests conducted in similar buildings, built in the same historical period. The variability range of the masonry characteristic, as well as the low values of Young modulus E and ultimate compression strength σ_u obtained for the adopted case studies, can be justified by the lack of standard processes for the production of bricks. This justifies the discrepancy of the results obtained by the surveys with respect to the ones recommended by the Italian standard regulation.

4. Dynamic characterization

As briefly mentioned above, a Monte Carlo-based stabilization diagram (MCSD) approach, as part of an Automated Operational Modal Analysis (AOMA) framework [36,37], was needed to perform the output-only dynamic identification of the two buildings in an unsupervised fashion. This procedure is well-established in the scientific literature, also explicitly for masonry structures [38]. In particular, the authors used Phase 1 of the recently published i-AOMA method [34] with the PoSER method [39] for mode merging. The i-AOMA method

Table 1

Results of the compression tests on concrete samples, where H_d is the hole depth, L is the specimen length, C_d is the carbonation depth, D is the diameter, ρ_c is the concrete density and f_c is the compressive strength.

Sample	Collection date	Location	H_d (cm)	L (cm)	C_d (cm)	D (mm)	ρ_c (kg/m ³)	f_c (MPa)	
Complex No. 1									
C1	First floor	Column	145	20.5	0	94	2196	12.9	
C2	First floor	Beam	–	18	5	94	2239	12.3	
C3	First floor	Column	75	22	2	94	2202	11	
C4	First floor	Beam	–	20	2	94	2238	11.8	
C5	Ground floor	Column	145	24	5	94	2189	11.1	
C6	Ground floor	Beam	145	22	12	94	2218	15.8	
C7	Ground floor	Column	155	28.5	7.3	94	2213	10.7	
C8	Ground floor	Beam	–	24	15	94	2284	13.9	
C9	Basement	Column	130	24	11	94	2216	11.3	
C10	Basement	Beam	–	22	10	94	2291	16.1	
C11	Basement	Column	140	23	23	94	2166	10.2	
C12	Basement	Beam	–	24	20	94	2170	10.8	
							Mean	2218.50	12.33
							Std.Dev.	39.47	1.98
Complex No. 2									
C1	Ground floor	Column	145	21.5	5	74	2276	10.1	
C2	Ground floor	Column	145	21.5	5	74	2301	9.4	
C3	Ground floor	Beam	145	20	5	74	2131	7.5	
C4	Ground floor	Beam	145	20	5	74	2157	8.2	
C5	Basement	Beam	145	94	22	94	2311	11.3	
C6	Basement	Beam	145	94	22	94	2308	11.6	
C7	Basement	Central	145	74	21	74	2281	16.5	
C8	Basement	Central	145	74	21	74	2279	16.6	
C9	First floor	Column	145	21	6	74	2274	13.2	
C10	First floor	Column	145	21	6	74	2273	13.8	
C11	First floor	Column	145	19	5.5	74	2355	12.5	
C12	First floor	Column	145	19	5.5	74	2351	12.3	
							Mean	2274.75	11.92
							Std.Dev.	67.39	2.89

Table 2

Results of the tensile tests on steel samples, where D_n is the nominal diameter, D_{eff} is the effective diameter, f_y is the yielding strength and f_u the ultimate strength.

Sample	Location	Element	Length (mm)	D_n (mm)	D_{eff} (mm)	f_y (MPa)	f_u (MPa)	
Complex No. 1								
A1	First floor	Column	515	30	29.94	287.5	409.6	
A2	First floor	Beam	520	24	23.81	277.9	385.82	
A3	Ground floor	Column	420	30	29.73	349.2	505.36	
A4	Ground floor	Beam	500	28	29.05	286.4	411.52	
A5	Basement	Column	550	30	29.76	260.45	352.14	
A6	Basement	Beam	550	30	29.81	263.7	395.15	
						Mean	287.53	409.93
						Std. Dev.	32.24	51.48
Complex No. 2								
A1	Ground floor	Column	505	21.79	21.79	268.69	422.15	
A2	Ground floor	Beam	515	19.76	19.76	314.74	436.82	
A3	Basement	Column	500	20.28	20.28	225.43	324.39	
A4	Basement	Beam	510	21.69	21.69	288.66	419.7	
A5	First floor	Column	450	17.77	17.77	253.31	355	
A6	First floor	Beam	570	9.58	9.58	232.55	312.11	
						Mean	263.90	378.36
						Std. Dev.	34.05	54.57

Table 3

Results of flat jack tests, where P is the jack pressure, σ_c the static stress, E_1 and E_2 the Young's moduli corresponding the first load and second load cycles, while σ_u is the compressive strength.

Test No.	P [MPa]	σ_c [MPa]	E_1 [MPa]	E_2 [MPa]	σ_u [MPa]	P [MPa]	σ_c [MPa]	E_1 [MPa]	E_2 [MPa]	σ_u [MPa]
Complex No. 1						Complex No. 2				
1	11.5	0.096	681.5	553.6	1.96	6.7	0.056	753	619	0.87
2	0	0				5	0.04			

applies to all structures, including CMB, offering significant advantages. Primarily, it reduces the arbitrariness in pole selection by providing an objective approach for mode estimation. This is achieved by merging the stabilization diagrams from multiple hyperparameter subsets until convergence. Additionally, the PoSER method, a well-established

technique in multi-setup OMA, is instrumental in identifying the partial mode shapes of the different setups and subsequently merging them to get the entire mode shapes. Six triaxial velocity sensors were used with a 4 Hz fundamental frequency, sensitivity of 20 V/(m/s), spectral noise of 5 ($\mu\text{V}/\text{Hz}^{0.5}$) and dynamic range of nearly 120 dB. Data acquisitions

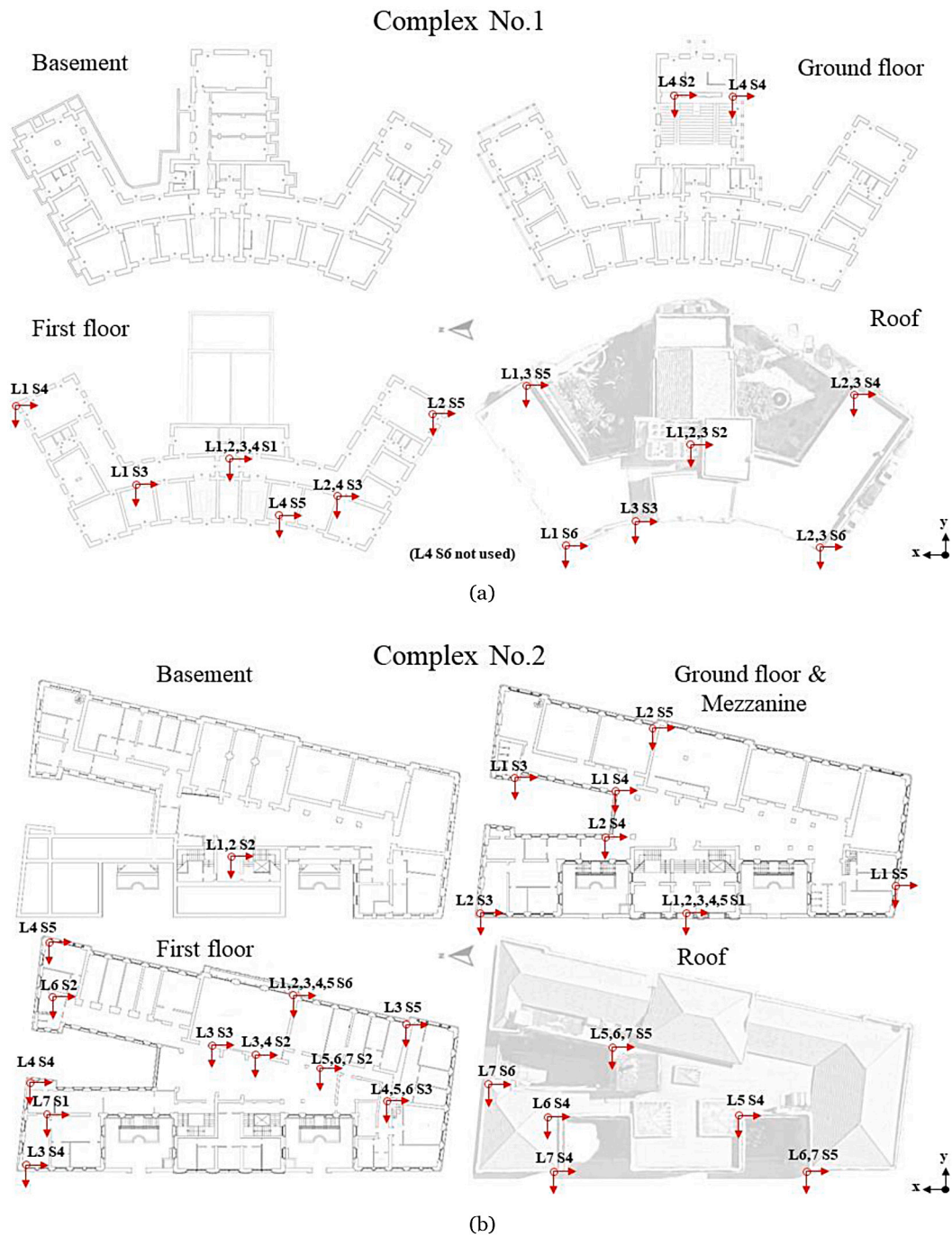


Fig. 6. Sensors' layout in (a) Complex No. 1 and (b) Complex No. 2. The numbers associated with each measurement point indicate the specific measurement setup to which the point belongs. In both cases, the x-axis is oriented N-S, while the y-axis is oriented E-W and the z-axis U-D.

were conducted for approximately 20 min per setup, with a sampling frequency of 100 Hz.

The sensor layouts for each complex are displayed in Fig. 6, resulting in 4 different setups for Complex No. 1 and 7 for Complex No. 2. The measurement points are indicated by the letter L (Layout) followed by the layout and Sensor (S) numbers. It should be remarked that these setups are the result of extensive preliminary works and stem from multiple practical considerations, which defined the minimum requirements for the instrumentation layout in the two complexes. First of all, the computed frequencies are sensitive to the location of the instrumentation, due to the mode shapes nodes and antinodes [40]. Hence, the sensors were mainly placed on the two top floors, where relatively higher vibration amplitudes were expected. However, not

all of them were clustered at the highest floors; some were placed on the ground floor (and on the mezzanine for Complex No. 2), to potentially capture higher bending modes. The sensors were also placed at the stiffest corners of the floors to avoid interference with the floor's vertical vibration. In general, locations at the outermost corners (both of the overall shape of the building and the single wings) were favourite, to better identify both global and local torsional movements. Due to the many similarities of the wings in both structures, it was also decided to not replicate the same sensor placement for all wings, as this was deemed too redundant. For Complex No. 2, it was also decided to dedicate a set of three channels to the basement, acting as control for all the others. Finally – but most importantly – all layouts had to be adjusted accounting for the limited quantity and length of the cables.

The resulting layouts were deemed as the ones necessary to thoroughly investigate the two complexes.

Modal parameters were obtained by merging all setups using the PoSER technique [39]. This led to identifying 14 points for Complex No. 1 and 25 for Complex No. 2. For Complex No. 1, the merging was performed considering L1,2,3,4 S1 has the sole reference sensor since it was shared among all four layouts. For Complex No. 2, due to the impossibility of covering all selected positions with the available cables, multiple reference sensors were applied in series. That is to say, L1,2,3,4,5 S1 (on the ground floor) and L1,2,3,4,5 S6 (on the first floor) were shared among the first five layouts (L1 to L5). The scaling constant was defined by solving a least squares problem considering both locations. Then, the resulting mode shapes were further re-scaled, to be merged with the modal coordinates obtained from L6 and L7. In these two cases, the reference points were moved (due to practical constraints) to L5,6,7 S2 (on the first floor) and L5,6,7 S5 (on the roof), which were both shared among the two last setups and the fifth layout.

The covariance values between recordings belonging to the same reference point on different layouts were used to assess the variability of the recordings; overall, for all points, directions, and layouts, it remained quite constant, in the order of magnitude of circa $0.01 - 0.05 \cdot 10^{-5}$ cm/s, where the variability of the signals themselves ranged between $0.1 - 0.5 \cdot 10^{-5}$ cm/s.

The investigations revealed relatively low excitation, as shown in Fig. 7. quantitatively, for Complex No. 1, the peak absolute velocity in the two horizontal directions – considering all layouts and acquisitions – never exceeded 0.035 cm/s (x-axis) and 0.037 cm/s (y-axis), while the vertical one was, obviously, even lower, at 0.015 cm/s. Similar values were encountered for Complex No. 2, with maximum velocities reaching 0.041 cm/s (x-axis), 0.038 cm/s (y-axis), and again 0.015 cm/s for the z-axis, as in the case of the first building. Of course, this might make the measures' quality relatively less reliable. Nevertheless, this was quite expected; indeed, this is the main advantage of using Operational Modal Analysis, i.e., to be able to identify the dynamic behaviour of the target systems from low-amplitude output vibrations only, as naturally caused by ambient vibration input [41].

For a quantitative measure, the average root mean square velocities were, for Complex No. 1 (mean \pm st.dev., considering the four setups separately), $0.0067 \pm 8.34 \cdot 10^{-4}$ cm/s for the channels oriented along x, $0.0064 \pm 3.89 \cdot 10^{-4}$ cm/s along y, and even just $0.0012 \pm 7.49 \cdot 10^{-5}$ cm/s along the vertical (z-axis). Complex No. 2 (considering the two setups) was only slightly more excited by the ambient vibrations, with $0.0099 \pm 3.79 \cdot 10^{-3}$ cm/s and $0.0100 \pm 4.31 \cdot 10^{-3}$ cm/s along the two horizontal directions (x and y, in the same order) and $0.0039 \pm 3.87 \cdot 10^{-3}$ cm/s on the z direction. Despite these generally low amplitudes, the algorithm used in this application was verified in previous applications to perform well even with lowly-excited output responses [34], comparable to the conditions found here.

The limited information content of the signals posed challenges in adopting classical covariance-based stochastic subspace identification (SSI-cov) or enhanced frequency domain decomposition (EFDD) techniques with predefined input parameters [39,42,43]. Therefore, the authors opted for a Monte Carlo-based stabilization diagram (MCSD) approach (Phase 1 of the i-AOMA method), which enabled mode identification by exploring the input parameter space of the SSI-cov.

The MCSD method builds upon the initial studies proposed by Zhou et al. in 2022 [44,45]. While the SSI-cov algorithm holds significant potential, the conventional practice of arbitrarily selecting input parameters can substantially impact the quality of dynamic identification results. This impact is particularly evident in the clarity and ease of detecting stable pole alignments associated with the natural frequencies of the analysed system, which are visually represented on a stabilization diagram (SD). Specifically, two crucial parameters of the SSI-cov algorithm come into play: the block row parameter, which dictates the dimensions of the Hankel matrix, and the maximum model order,

which governs the exploration of the system's order, often unknown, thereby influencing the vertical axis dimensions of the SD.

In the initial studies by Zhou et al. [44,45], and subsequently implemented as Phase 1 of the i-AOMA method by Rosso et al. in 2023 [34], a Monte Carlo (MC) approach was employed to explore various input parameter values, eliminating the need for arbitrary and potentially suboptimal manual selections.

Specifically, the MCSD procedure introduces two additional governing parameters: a time window length that extracts a specific portion of the recorded vibration signals, and a time instant parameter that determines the position of this time window within the entire monitored signal. These parameters are introduced to address a fundamental assumption. Despite focusing on a particular portion of the recorded signals obtained from the vibration response of the same structural system, they are expected to contain all the information related to the system's dynamics. Therefore, when random segments of the signals undergo the SSI-cov algorithm, the stable poles corresponding to the actual physical modes of the system should consistently emerge. In contrast, those associated with spurious modes should only occasionally appear.

With the MCSD approach, the user only needs to specify the number of MC simulations in which various sets of the four considered governing parameters are sampled and perform post-processing on all the results derived from the stabilization diagrams (SDs).

In Phase 1 of the i-AOMA method, these results are overlaid onto a comprehensive stabilization diagram, enabling the identification of recurring stable pole alignments even through simple visual inspection. Furthermore, to offer a more distinct overview of these recurring stable pole alignments and facilitate the identification of the likely physical natural frequencies of the studied system, Phase 1 of the i-AOMA method employs post-processing of the overlaid SD using the kernel density estimation algorithm [46]. The peaks in the kernel density are then associated with the most frequently occurring stable poles, thereby identifying the system's natural frequencies.

As [44,45] recommended using a minimum of 100 MC simulations, this study has opted for an increased number of 250 MC simulations to enhance the reliability of the identified peaks in the kernel density graph.

Specifically, the Halton technique [47,48] is adopted to generate quasi-random samples of the control parameters for the SSI-cov within the corresponding ranges. Taking into consideration the existing literature [44,49,50], the bounded ranges for these control parameters are defined as follows:

$$n \in [n_{min}, n_{max}] = [2 \cdot l, i_{max} \cdot l], \quad (1)$$

$$j \in [j_{min}, j_{max}] = \left[\left\lceil \frac{2}{\max\{f_f, 1\}} \right\rceil, j_{max} \cdot l \right], \quad (2)$$

$$t \in [t_{min}, t_{max}] = [0, j_{max}], \quad (3)$$

$$i \in [i_{min}, i_{max}] = \left[\left\lceil \frac{f_s}{2 \max\{f_f, 1\}} \right\rceil, 10 \left\lceil \frac{f_s}{2 \max\{f_f, 1\}} \right\rceil \right], \quad (4)$$

where these four parameters represent the maximum model order n , the time window length j , the time target t concerning which the time window is centred [44], and the time shift parameter i . $\lceil \cdot \rceil$ is the rounding operation to the nearest integer, l is the time shift, and f_f the fundamental frequency (which is estimated using the singular value decomposition of the power spectral density as suggested by Zhou and Li [44]). The SDs resulting from the s successful quasi-Monte Carlo simulations are overlapped. The following stability criteria are considered [39]:

$$\Delta f = \frac{f_a - f_b}{f_a} \leq 0.01 \quad (5)$$

$$\Delta \xi = \frac{\xi_a - \xi_b}{\xi_a} \leq 0.05 \quad (6)$$

$$1 - \text{MAC}(\psi_a, \psi_b) \leq 0.02 \quad (7)$$

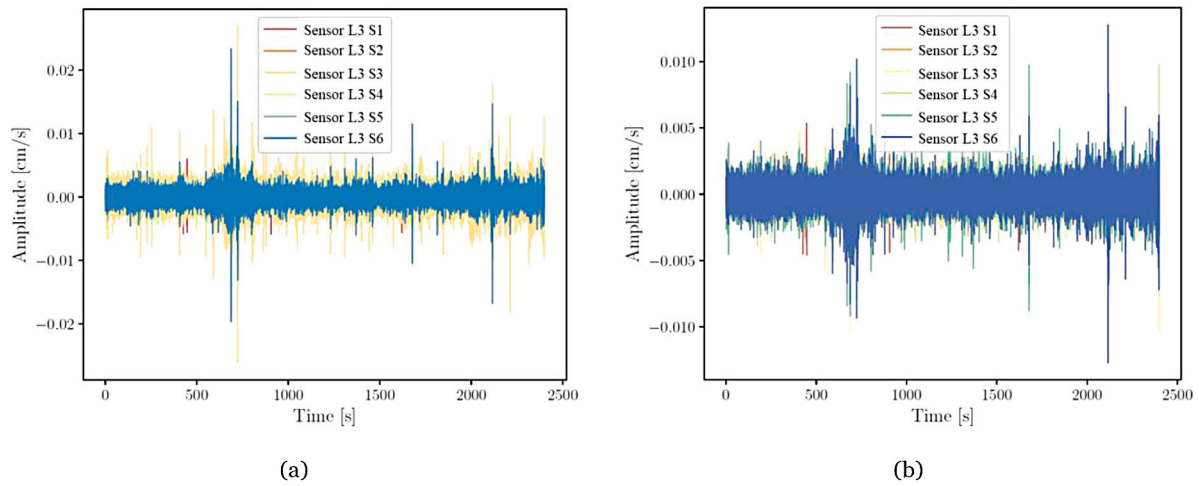


Fig. 7. Superposition of sensor records for Complex No. 1 along the (a) N-S and (b) E-W directions. Based on acquisitions from the third setup (L3) considering all the six sensors (S1-S6).

$$\xi_a \leq 0.1 \tag{8}$$

The subscripts a, b represent two poles in the SD, and MAC is the modal assurance criterion (which represents the correlation between two modal vectors [39]). Particularly, Eqs. (5)–(7) are denoted as soft criteria (SC) in terms of frequency, damping, and mode shape, respectively, whereas Eq. (8) is designated as hard criterion (HC) on the damping range [51]. The extraction of physical poles from possibly stable poles is accomplished via Kernel Density Estimation (KDE). The authors adopted a Gaussian Kernel [52,53]. The data consists of all the possible stable poles N_p within the comprehensive SD, considered a univariate dataset along the frequency axis only. Therefore, the univariate KDE based on a Gaussian kernel can be written as follows:

$$\hat{\phi} = \frac{1}{N_p h} \sum_{p=1}^{N_p} K \left(\frac{z - z_p}{h} \right), \tag{9}$$

where

$$K \left(\frac{z - z_p}{h} \right) = \frac{1}{\sqrt{2\pi}h} e^{-\frac{(z-z_p)^2}{2h^2}}. \tag{10}$$

The parameter h in Eqs. (9)–(10) is known as bandwidth (BW) or smoothing parameter, and it is typically fixed across the entire sample [52]. Since the BW definition has a significant impact, a user-dependent definition of its value should be avoided in automatic applications. Therefore, the improved Sheather-Jones (ISJ) algorithm [54, 55] is adopted to define the bandwidth automatically.

Fig. 8 showcases the overlay of all the stabilization diagrams (SDs). In contrast, Fig. 9 presents the kernel density graph resulting from post-processing the overlaid SDs, focusing solely on the fully stable poles. More in detail, Fig. 9 shows the Kernel Density Estimation of the overlapped stabilization diagrams for (a) Complex No. 1 and (b) 2 following the MCSD approach [34].

Table 4 provides the first three modal parameters for Complex No. 1 and Complex No. 2, specifically the natural frequency (f) and modal damping (ξ). The higher modes were not considered due to difficulties interpreting the mode shapes with the current sensor layouts. Additionally, the mode at 2.59 Hz for Complex No. 2 was not considered reliable. This is because the velocimeter can only be used for identifying frequencies above its own natural frequency of 4 Hz. Therefore, the authors cannot confidently assert that modes below 4 Hz reflect the actual physical characteristics of the structure. For Complex No. 1, the first mode has a natural frequency of 5.07 Hz with a relatively low damping ratio of 0.11%. The natural frequencies increase as we progress to higher modes while the damping ratios remain pretty low. This suggests Complex No. 1 exhibits a predominantly rigid and lightly

Table 4
Modal parameters of the first three modes of Complex No. 1 and Complex No. 2, where f is the natural frequency and ξ is the modal damping.

Mode	Complex No. 1		Complex No. 2	
	f [Hz]	ξ [%]	f [Hz]	ξ [%]
1st	5.07	0.11	5.76	1.20
2nd	6.49	4.23	6.38	2.33
3rd	8.04	0.87	7.09	2.45

damped response. For Complex No. 2, The first mode has a slightly higher natural frequency of 5.76 Hz compared to Complex No. 1. As we move to higher modes, the natural frequencies and damping ratios for Complex No. 2 are generally lower than those of Complex No. 1.

Interpreting the mode shapes for both buildings presents significant challenges. This is also due to the complex geometry of the two large buildings. For this aim, the Authors opted to use oriented arrows, proportional to the mode shape components, to avoid overlap between the wireframe’s undeformed and deformed states. The undeformed state serves as a background reference, aiding in understanding the predominant direction of deformation. Only the first three modes, depicted in Fig. 10, exhibit a noticeable deformation concentration. In the case of Complex No. 1, the first mode exhibits a pure torsional behaviour, more evident at the last floor of the structure. The second mode is a global translational one along the symmetry axis (Y-axis). Finally, the last mode results primarily a translation mode along the X-axis with a torsional component.

Similarly, Complex No. 2’s first mode represents a global torsional mode, the second is mainly translational along the East-West direction (Y-axis), while the third mode represents a global translation mode along the North-South direction (X-axis).

The higher modes were not represented due to the complexities involved in interpreting these modes with the current sensor setups.

5. Finite element model development and calibration

This section explores the FE model’s development and presents the model calibration outcomes. The authors will discuss both buildings together rather than sequentially, as they share similar characteristics. This phase’s modelling activities adhere to Italian regulations [56].

5.1. FE model

The FE model implementation started with a high-fidelity geometric survey based on a 3D laser scanner; see Fig. 11. The authors created

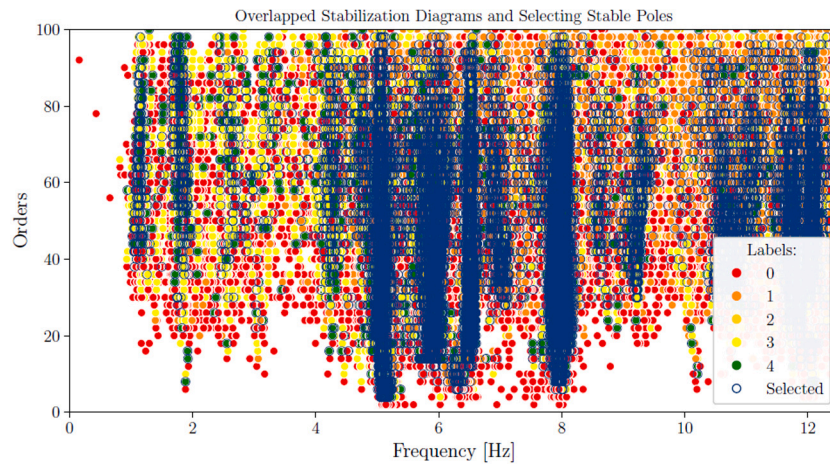


Fig. 8. Overlap of the stabilization diagrams for Complex No. 1 flowing the MCSD method [34]. The labels from 0 to 4 indicate (0) unstable, (1) stable in frequency, (3) stable in frequency and damping, (4) stable in frequency and mode shape and (5) stable in frequency, damping and mode shape respectively.

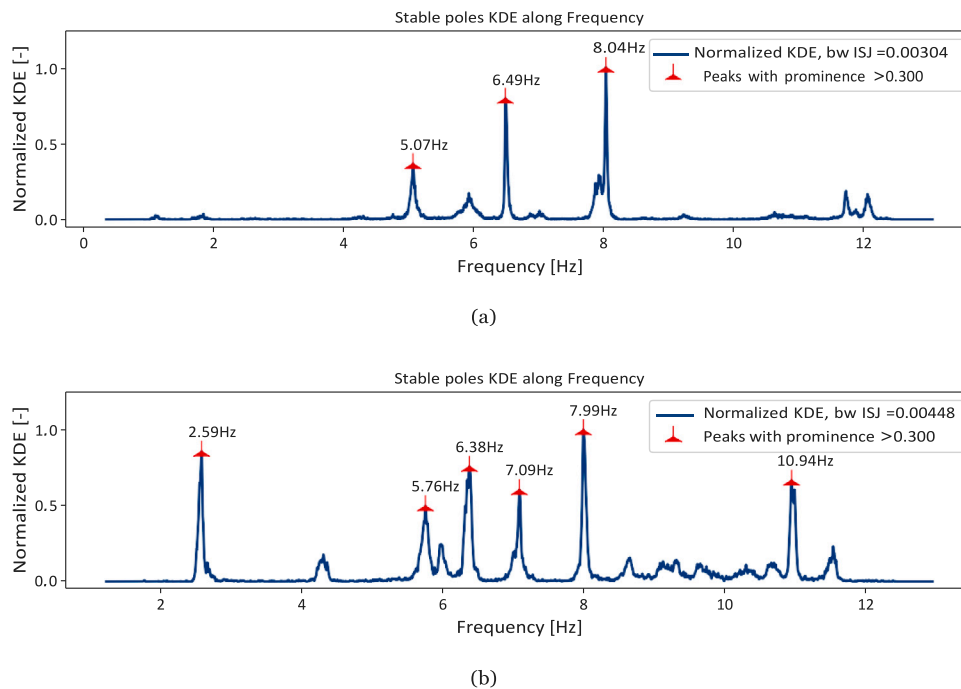


Fig. 9. Kernel Density Estimation of the overlapped stabilization diagrams for (a) Complex No. 1 and (b) 2.

a Building Information Model (BIM) using Autodesk Revit software, leveraging the data from the graphical drawings and the 3D laser scanner survey. This approach enabled the development of a high-fidelity structural model, facilitating the import into the chosen finite element analysis software, SAP2000.

Fig. 12 shows two Revit model representations of (a) Complex No. 1 and (b) Complex No. 2.

By following this procedure, all the nodes and structural elements were automatically recognized by the FEM software. The model of Complex No. 1 consists of 2057 nodes, 113 *beam* elements, and 73 *shell* elements. Conversely, the model of Complex No. 2 consists of 2000 nodes, 126 *beam* elements, and 87 *shell* elements.

The following modelling assumptions have been adopted:

- All masonry, both perimeter and internal walls, were modelled using *shell* elements, with each element's dimensions taken from on-site measurements or obtained from the graphical drawings provided. Fully consistency between the vertical or horizontal

confinement elements (i.e. columns and beams integrated into the masonry) with *shell* elements has been guaranteed through a proper discretization.

- Vertical elements were modelled using *beam* elements, whether isolated columns or the confinement elements integrated into the masonry, contributing to the confinement frame definition.
- The stiffness contribution of the stairs was indirectly considered with calibrated body constraints between nodes of anchorage lying on floors of competence at different heights. Moreover, the mass of the stairs was uniformly distributed and split over the floor of competence.
- The floor was modelled as a *membrane* element with a thickness of 23 cm, obtained from an inertial equivalence procedure performed by considering a rigid full concrete slab of 20 cm stiffened by thick beams. The rigid connection between the *membrane* elements and vertical walls (*shell* elements) or columns (*beam* elements) was guaranteed by linking the mesh joint of the latter with the control point adopted for the former. In order to reduce

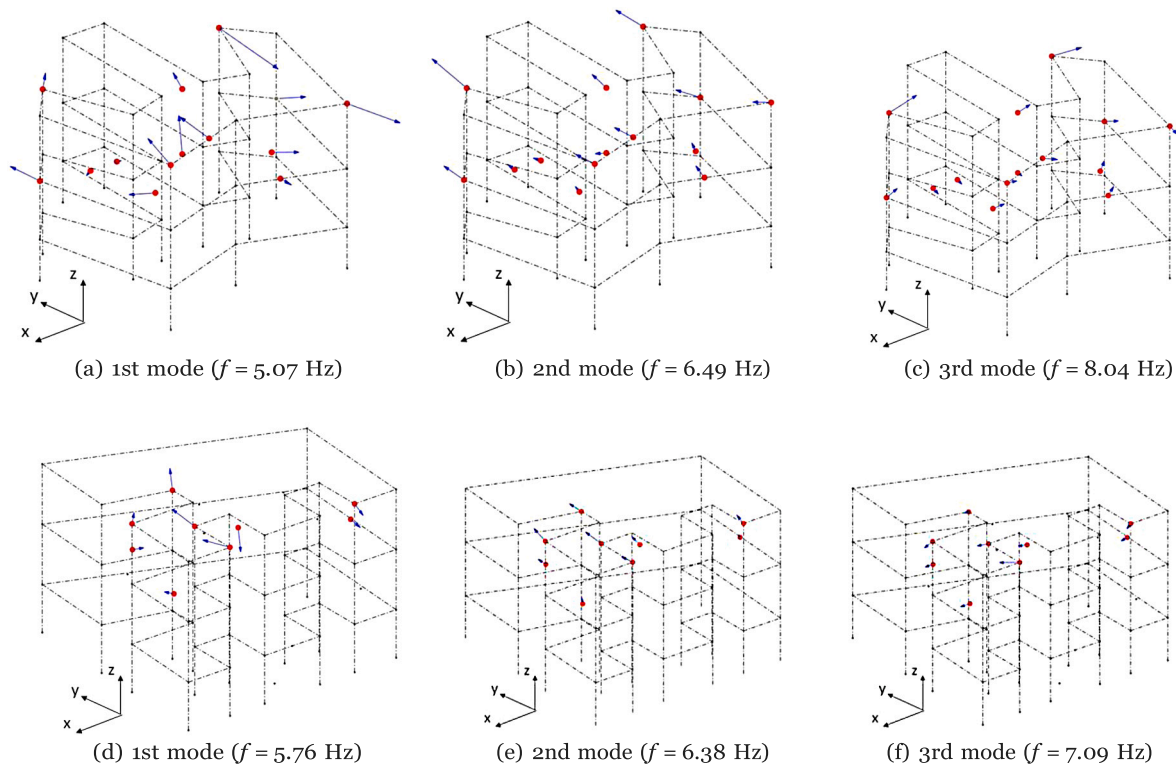


Fig. 10. Experimental mode shapes for (a)–(c) Complex No. 1 and (d)–(f) Complex No. 2.



Fig. 11. Point cloud obtained with the 3D laser scanner.

the computational effort during the optimization routine and prevent local modes of the slabs, the modelling of the floors as shells was avoided. The membrane, in fact, represents an efficient modelling strategy for reproducing faithfully the real distribution of masses and stiffness of the structures. Additionally, the rigid behaviour of the floor has been guaranteed by adopting a *daphragm* constraints applied to all the nodes that live on the same floor. The feasibility of the proposed modelling approach has been proved by comparing the modal modes and shapes obtained from the two models.

- All nodes in the RC frame (columns and beams as well as horizontal and vertical reinforcement elements of the CM) were modelled as fully restrained joints, in line with typical assumptions for reinforced concrete frame structures. Hence, rigid connections between beams and columns were established, ensured by the

presence of masonry walls supporting the beams, preventing flexural rotations. According to the information obtained from the historical survey, which reports the presence of single-sloped footing, the foundation was modelled as fully restrained boundaries at the bottom edge of the columns of the basement floor. This assumption satisfied also the recommendation provided by the Italian regulation, which allows for avoiding the modelling of the foundation if rigid connections (e.g. wall footing and/or simple spread footing) and consistent mechanical behaviour of the soil are identified.

- The pressure of the soil against the façade of the basement was not considered because out of the scope of the present research. However, its confining effect on the masonry was modelled by providing external horizontal restrains along the perimeter of the basement floor, coherently to the slope of the ground level around the building.

The model does not consider steel rebars, whose contribution is negligible to the performed analysis, and in fact is normally disregarded. The loading conditions of the model include the dead weight of all structural elements (e.g. masonry, vertical elements), which was evaluated by multiplying the known value of the concrete mass density, equal to 25 kN/m^3 , by the equivalent slab thickness equal to 0.22 m . Differently from all the structural elements directly modelled and their mass automatically considered by the software during the modal analysis, the dead loads of floors have been modelled as gravitational loads because the adoption of zero-thickness and zero-mass *membrane* element in place of *shell*.

The non-structural load, G_2 , was expressed in terms of two contributions. The non-structural loads, G_2^I , referred to the weight of the pavement, set equal to 0.8 kN/m^2 for the floors and 0.5 kN/m^2 for the roof, respectively. Both values are mainly representative of the pavement layers of each floor for which the authors had no detailed information deriving from historical drawings or recent surveys. Finally, an additional permanent non-structural load, G_2^{II} , of 0.8 kN/m^2 ,

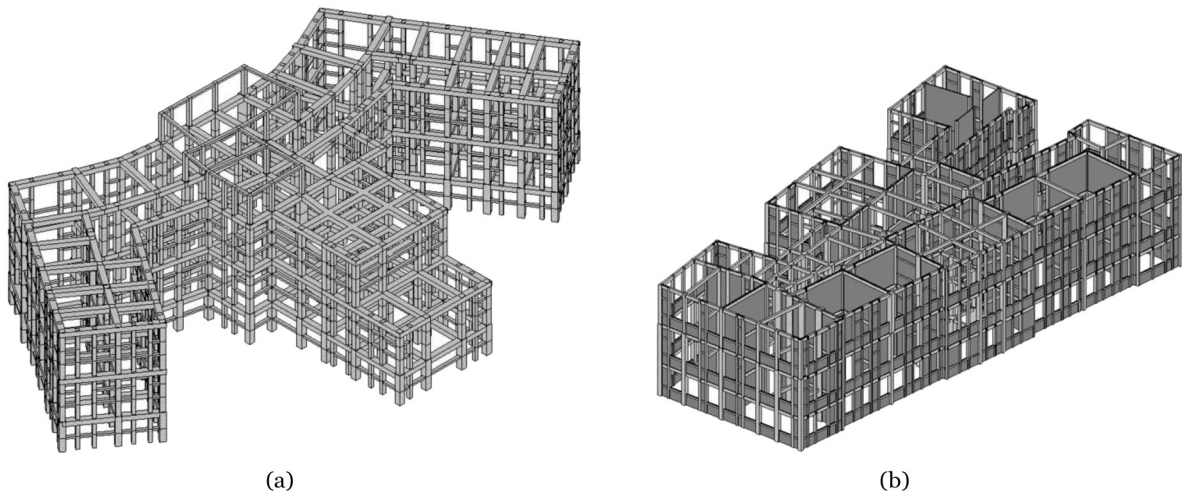


Fig. 12. Revit model representations of (a) Complex No. 1 and (b) Complex No. 2.

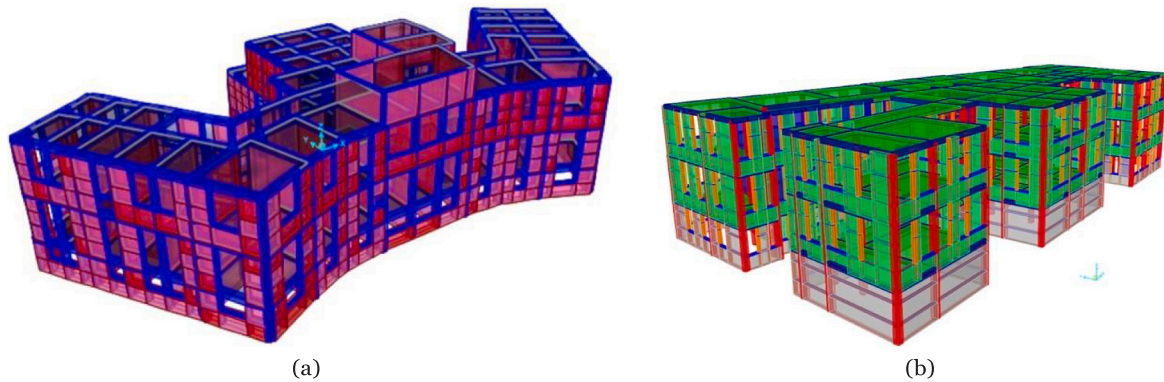


Fig. 13. Extruded representations of the FE models of (a) Complex No. 1 and (b) Complex No. 2.

according to the recommendations provided by the Italian regulation and coherent to the intended use of the building, was considered to account for partitions and equipment.

All model elements were modelled as linear elastic. Fig. 13 shows two views of the FE models of Complex No. 1 and 2, respectively.

The authors optimized all modelling parameters except the RC weight assumed equal to 2500 kg/m^3 . The list of unknown parameters is as follows:

- Young's modulus of masonry E_m ;
- Specific weight of masonry ρ_m ;
- Young's modulus of concrete ρ_c ;
- Equivalent area of the RC stiffening elements A_{RC} ;
- Non-structural weight increment ΔG_2 intended as the sum of both the contributions of the non-structural permanent dead weight of the pavement structure (ΔG_2^I) and that one provided by partitions and equipment (ΔG_2^{II}). This value must be considered as a positive or negative increment with respect to the reference value of G_2 assumed since the beginning of the optimization.;

The five parameters exhibit significant uncertainties. This includes not only Young's modulus and the specific weight of masonry, which typically display considerable variability, but also the size and stiffness of the RC frames, which are relatively uncertain for two reasons. Firstly, the concrete is in an early stage of development, with low compression strength and considerable spatial scatter. Secondly, the size of the frames is not consistently constant, as concrete was poured without formwork, resulting in voids within the masonry. Additionally, as is typical, it is challenging to precisely quantify the permanent

nonstructural weight, which has been included in the list of unknown parameters.

5.2. Model calibration

The model calibration has been carried out by solving the following optimization

$$\hat{x} = \arg \min_x \sum_{i=1}^N \left(\frac{f_i^{\text{num}} - f_i^{\text{exp}}}{f_i^{\text{exp}}} \right)^2 \quad (11)$$

where \hat{x} is the vector of optimized parameters, N is the number of considered modes, f_i^{num} and f_i^{exp} are the numerical and experimental natural frequencies, Φ_i^{num} and Φ_i^{exp} are the i th experimental and numerical modes, respectively.

In this way, the sum of the differences between the target frequencies and the experimental ones has been evaluated at each iteration by associating the corresponding modal shape through the relative mass participation factor.

The optimization has been solved using the metaheuristic Genetic Algorithm (GA) [57]. The GA is a stochastic optimization technique inspired by the principles of Darwinian evolution. It is used to find approximate solutions to complex search and optimization problems. In a GA, a population (individuals) of potential solutions (represented as chromosomes and genes) evolves over generations. The algorithm applies genetic operators like selection, crossover (recombination), and mutation to create new individuals. Through repeated generations, the algorithm seeks to improve the quality of solutions by favouring

Table 5
List of upper and lower bounds and optimized model parameters for Complex No. 1 and 2, respectively.

Parameter	Complex No. 1			Complex No. 2		
	Lower bound	Upper bound	Optimum	Lower bound	Upper bound	Optimum
E_m [MPa]	800	2000	1950	600	1800	1650
ρ_m [kg/m ³]	1400	2200	1500	1400	2200	1500
E_c [MPa]	26 000	35 000	30 100	26 000	35 000	28 900
A_{RC} [cm ²]	225(15 × 15)	1600(40 × 40)	900	225(15 × 15)	1600(40 × 40)	900
ΔG_2 [kN/m ²]	-1.0	1.0	-0.1	-1.0	1.0	-0.3

individuals with better fitness. GAs are beneficial for exploring large solution spaces, like the current application, and finding global optima.

In this work, a modified real-coded GA has been adopted to match the optimization process's final target. It has been set to a population size of 200 individuals, while the selection of the parents has been performed by using a standard Roulette Wheel selection in which the individual with the highest fitness has a higher probability of being selected [58]. In order to increase the exploration and exploitation capability of the algorithm, a single-point guided crossover operator has been implemented based on the probability pointed out by the Roulette Wheel [59]. In other words, once the parent generation is obtained, the exchange of genes (design variables of the problem) for the definition of the children is encouraged between individuals marked with high fitness. Finally, to avoid being trapped in local optimal solutions, a random mutation for each gene of the chromosome has been performed with an activation probability of 5%.

The optimal set of five parameters obtained from the GA optimization process is presented in Table 5. Notably, all of these optimal parameters fall within the input parameter bounds.

The optimized values for the masonry weight (ρ_m) and concrete Young's modulus (E_c) fall within the expected range of typical values for masonry and RC, respectively. More in detail, with specific regard to the mechanical properties indicated by E_m and ρ_m , the upper bounds have been defined according to the suggested thresholds provided by the Italian Standard Regulation NTC2018 while the lower bounds have been fixed, aiming to include the results obtained by the experimental campaign.

However, it is noteworthy that Young's modulus of masonry in the optimization results exhibits significantly higher values than the 600 to 700 MPa range obtained from flat jack tests. There is a significant discrepancy between the optimal E_m values and that obtained from double flat jack tests for both buildings. However, the latter values can be considered representative of the secant stiffness, while the one obtained from the updating can be more associated with the initial stiffness. For instance, the stress-strain curve for the flat jack tests conducted in Complex No. 2, resulted in Young's modulus tangent to zero equal to 1457, nearly twice as high as the experimental secant value of 753. This fact demonstrates that the stiffness at low vibration levels is between 2–3 times higher than that obtained from the standard flat jack test estimations. The same observation can be adopted for the experimental tests conducted on complex No. 1.

Notably, optimization results are influenced by the input data's accuracy, the numerical model's fidelity, and the assumptions made during the optimization process. Therefore, the optimized parameters should not be interpreted as an absolute representation of material properties. The optimization process considers a simplified numerical model of the structure, which may not capture all the complexities of real-world behaviour. It assumes linear elastic material properties, whereas the actual behaviour of masonry can be more complex due to factors like cracking, joint properties, and material heterogeneity. Additionally, the optimization algorithm aims to find the best fit between the numerical model and experimental modal data. The algorithm may converge to parameter values that minimize the difference between the model and experimental data, even if they do not match the physical properties exactly.

The cross-sectional area of RC elements consistently exceeds the average cross-section, typically around 20 × 20 cm. This could be

Table 6
Comparison between experimental and optimized numerical modal parameters, where f is the natural frequency.

Complex	Numerical f [Hz]	Experimental f [Hz]	Relative difference
No. 1	4.92	5.07	-2.91%
	6.89	6.49	6.16%
	7.82	8.04	-2.74%
No. 2	5.01	5.76	-13.02%
	6.16	6.38	-3.30%
	6.53	7.09	-7.81%

attributed to the irregular shape of the frame, which induces additional mechanical interaction between the RC frame and masonry. The protrusions of the RC frame create a stiffening effect on the CM structure. Concerning the additional permanent non-structural load, it is essential to note that it is significantly higher than what is recommended by national regulations. This additional load is associated with the flooring and furniture.

Table 6 provides a comparative analysis of the numerical and experimental modal parameters for Complex No. 1 and Complex No. 2.

Figs. 14 and 15 show a 3D representation of the first three optimized modes of Complex No. 1 and 2, respectively.

The three modes are pretty analogous in the two structures. The first mode consistently exhibits global torsional behaviour while the second and third modes are translational along the minor and higher inertia direction, respectively. With specific regard to the third mode, a no-negligible mass participation factor of about 10% for the torsional component, for both complex No. 1 and No. 2, has been also recognized, consistently with the corresponding experimental hybrid modal shape observed.

For Complex No. 1, the numerical natural frequencies are slightly lower than the experimental values for the first mode (3.05% lower) and the second mode (3.99% higher). However, there is a significant deviation for the third mode, with the numerical value being 16.69% lower than the experimental value. The authors found difficulties in achieving a good agreement between mode shapes. For Complex No. 2, again, three modes are compared. The numerical natural frequencies are consistently lower than the experimental values, with differences of 13.02%, 3.30%, and 7.81% for the first, second, and third modes, respectively. These discrepancies suggest that the numerical model may underestimate the frequencies for Complex No. 2, especially for the third mode.

Structural complexity and modelling assumptions are the primary factors contributing to the limited agreement between mode shapes. Additionally, the experimental records were not highly informative, primarily due to the low excitation level, possibly leading to measurement errors during the mode merging.

5.3. Discussion

It has been found that only the first three modes exhibit significant deformation concentration, indicating the complex dynamic behaviour of the buildings under investigation. The optimization revealed that only few parameters, such as Young's modulus of concrete

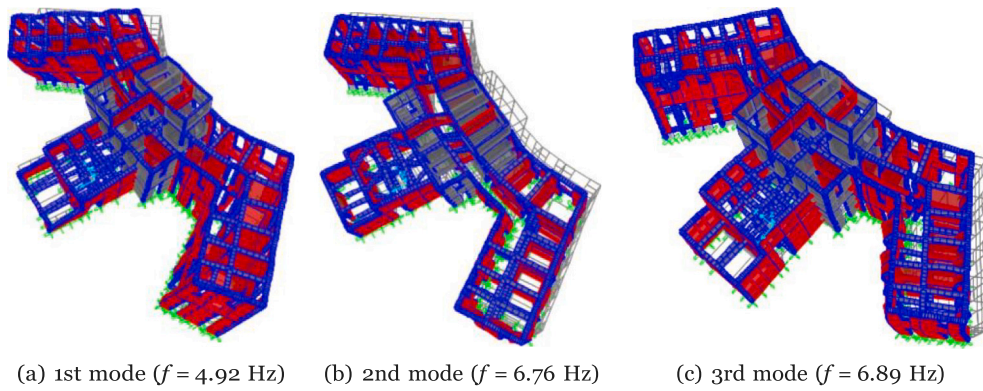


Fig. 14. 3D representation of the first three modes of the optimized numerical model of Complex No. 1.

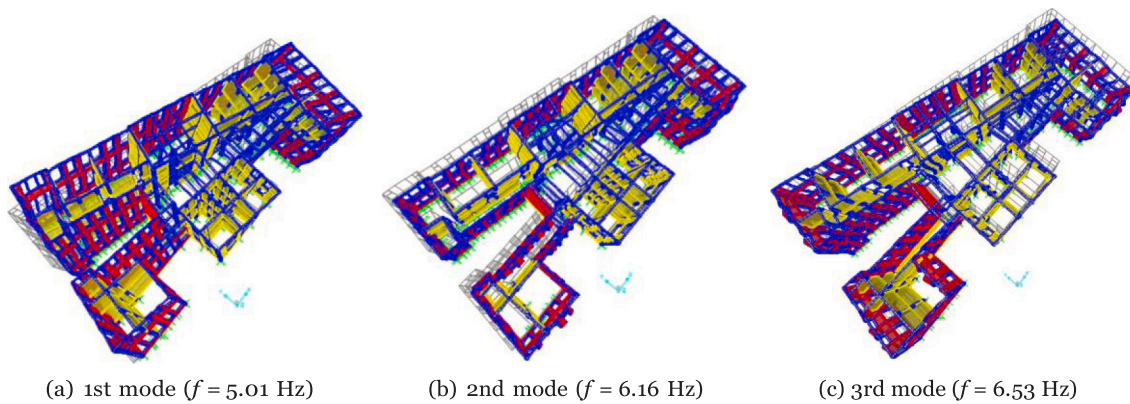


Fig. 15. 3D representation of the first three modes of the optimized numerical model of Complex No. 2.

and the masonry weight, fall within the expected ranges for masonry and RC materials. Young's masonry modulus is significantly higher than the values obtained from flat jack tests. This discrepancy raises important questions regarding the structural complexity of confined masonry (CM) buildings and the assumptions made during the modelling process.

It should be remarked that the optimized parameters derived from this study should not be interpreted as direct representations of the mechanical properties of masonry. Instead, they serve as equivalent modelling parameters, considering the complexities of modelling and measurement errors. These parameters act as effective surrogates, allowing for a better fit between numerical simulations and experimental modal parameters.

In a broader context, it is worth noting that when modelling CM structures, the added reinforced concrete ties introduce a substantial stiffening effect that cannot be adequately captured using conventional frame and shell elements alone. The interaction between masonry and RC frames extends across their entire contact surfaces, not limiting to the traditional nodal contact points typically considered in finite element (FE) modelling. Furthermore, how RC frames are constructed, poured directly into the voids left by masonry, leads to protrusions that result in increased compliance. This effect justifies the higher values assigned to Young's modulus of masonry and the corresponding adjustments in equivalent cross-sectional properties.

Therefore, the current modelling choices, typical in engineering practice, lead to a substantial underestimation of the masonry-RC interaction, which should be compensated by the higher stiffness of the masonry panels to achieve a reasonable estimate of the dynamic behaviour.

6. Conclusions

This paper investigates the dynamic characteristics and model updating of two confined masonry (CM) complexes at the University of Messina, constructed in the aftermath of the devastating 1908 earthquake. CM has emerged as a prominent structural system in post-earthquake reconstruction. However, the scientific literature offers limited insight into their dynamic characterization and the modelling challenges associated with such complex structures.

The research is grounded in a comprehensive examination of these buildings, including destructive tests on materials like reinforced concrete, masonry, and steel. Additionally, dynamic identification is conducted using the Monte Carlo-based stabilization diagram (MCSD), i.e. the Phase 1 of the recently published Intelligent Automated Operational Modal Analysis (i-AOMA) method.

Modal analysis reveals that interpreting mode shapes for these structures is complex, with only the first three modes exhibiting significant deformation concentration. More in detail, the first mode is pure torsional while the second and third ones are primarily translational along the minor (Y-axis) and higher (X-axis) inertia axis, respectively. With specific regard to the third numerical mode, a non-negligible torsional deformation has been detected consistently with the experimental modal shapes observed.

The finite element (FE) modelling was based on a 3D laser scanner and a BIM model. The structural model used frame elements for reinforced concrete (RC) components and shell elements for masonry panels.

A Genetic optimization algorithm was implemented to fine-tune five modelling parameters and achieve the best agreement between experimental and numerical modal parameters. Some parameters, such as Young's modulus of concrete and the masonry weight, align with

typical ranges for masonry and RC. However, it is observed that Young's modulus for masonry significantly exceeds values obtained from flat jack tests, which raises questions regarding structural complexity and modelling assumptions.

It is crucial to emphasize that the optimized parameters should not be interpreted as direct representations of the mechanical properties of masonry. Instead, they are equivalent modelling parameters, accounting for modelling and measurement errors. In the broader context, it is worth noting that masonry introduces a substantial stiffening effect that cannot be adequately captured with conventional frame and shell elements. Masonry and RC frames interact along their entire contact surfaces, extending beyond nodal contact points between FE elements. This interaction is further accentuated by the traditional method of pouring RC frames directly into the voids left by masonry, resulting in protrusions that contribute to higher compliance and justify the elevated values for Young's modulus of masonry and the increased equivalent cross-section.

Future research efforts will focus on cross-validating the outcomes of the metaheuristic optimization by employing other optimization algorithms. Furthermore, the authors intend to expand the number of flat jack tests to achieve a more comprehensive assessment of the masonry properties within the considered building.

CRedit authorship contribution statement

Raffaele Cucuzza: Writing – review & editing, Writing – original draft, Visualization, Validation, Software, Resources, Methodology, Investigation, Formal analysis, Data curation. **Marco Civera:** Writing – review & editing, Writing – original draft, Validation, Investigation, Formal analysis, Data curation. **Angelo Aloisio:** Writing – review & editing, Writing – original draft, Software, Methodology, Investigation. **Giuseppe Ricciardi:** Resources, Methodology, Conceptualization. **Marco Domaneschi:** Writing – review & editing, Writing – original draft, Validation, Supervision, Project administration, Methodology, Investigation, Funding acquisition, Formal analysis, Data curation, Conceptualization.

Declaration of competing interest

The authors declare that they have no known competing financial interests or personal relationships that could have appeared to influence the work reported in this paper.

Data availability

Data will be made available on request.

Acknowledgements

The support of the SISCON (Safety for InfraStructures and CONstructions), Interdepartmental Center of the Politecnico di Torino, and its Coordinator, Prof. Bernardino Chiaia, is gratefully acknowledged. Prof. Giuseppe Carlo Marano and Prof. Valentina Villa of the Politecnico di Torino are also gratefully acknowledged. The authors are also grateful to Prof. Ornella Fiandaca and Dr. Alessandra Cernaro of the University of Messina for providing the graphical drawings and the laser scanner survey. Finally, the support given by Eng. Marco Martino Rosso during the interpretation of the experimental results for the dynamic characterization with the AOMA method is gratefully acknowledged.

References

- [1] Borah B, Singhal V, Kaushik H. Sustainable housing using confined masonry buildings. *SN Appl Sci* 2019;1(9). <http://dx.doi.org/10.1007/s42452-019-1020-4>, cited By 19.
- [2] Singhal V, Rai D. In-plane and out-of-plane behavior of confined masonry walls for various toothing and openings details and prediction of their strength and stiffness. *Earthq Eng Struct Dyn* 2016;45(15):2551–69. <http://dx.doi.org/10.1002/eqe.2783>, cited By 38.
- [3] Matošević D, Sigmund V, Guljaš I. Cyclic testing of single bay confined masonry walls with various connection details. *Bull Earthq Eng* 2015;13(2):565–86. <http://dx.doi.org/10.1007/s10518-014-9627-8>, cited By 22.
- [4] Marques R, Lourenço P. Structural behaviour and design rules of confined masonry walls: Review and proposals. *Constr Build Mater* 2019;217:137–55. <http://dx.doi.org/10.1016/j.conbuildmat.2019.04.266>.
- [5] Brzev S. Earthquake resistant confined masonry construction. In: *Earthquake-resistant confined masonry construction*. 2007.
- [6] Meli R, Brzev S, Astroza M, Boen T, Crisafulli F, Dai J, Farsi M, Hart T, Mebarki A, Moghadam A, Quiun D, Tomazevic M, Yamin L. Seismic design guide for low-rise confined masonry buildings. In: *Seismic design guide for low-rise confined masonry buildings*. 2011, cited By 79.
- [7] Ourenço P. Current experimental and numerical issues in masonry research. In: *Proc 6th national conference on seismology and seismic engineering*. 2004, p. 119–36, URL <http://www.civil.uminho.pt/masonry>.
- [8] Tomaževič M, Klemenc I. Seismic behaviour of confined masonry walls. *Earthq Eng Struct Dyn* 1997;26(10):1059–71.
- [9] Tomaževič M. *Earthquake-resistant design of masonry buildings*. Imperial College Press; 1999.
- [10] Yekrangnia M. Effects of RC ties on seismic performance improvement of confined masonry walls under combined in-plane, out-of-plane, and vertical loads. *Eng Struct* 2023;293:116648.
- [11] Galvis F, Miranda E, Heresi P, Dávalos H, Ruiz-García J. Overview of collapsed buildings in Mexico City after the 19 September 2017 (Mw7.1) earthquake. *Earthq Spectra* 2020;36:83–109. <http://dx.doi.org/10.1177/8755293020936694>.
- [12] Ahmad N. A note on the strong ground motions and behavior of buildings during 26th Oct. In: 2015 Afghanistan-pakistan earthquake. Oakland, CA: Earthquake Engineering Research Institute; 2015, cited By 1.
- [13] Tarque N, Pancca-Calsin E. Building constructions characteristics and mechanical properties of confined masonry walls in San Miguel (Puno-Peru). *J Build Eng* 2022;45:103540.
- [14] Ruiz-García J, Negrete M. Drift-based fragility assessment of confined masonry walls in seismic zones. *Eng Struct* 2009;31(1):170–81.
- [15] Lovon H, Tarque N, Silva V, Yepes-Estrada C. Development of fragility curves for confined masonry buildings in Lima, Peru. *Earthq Spectra* 2018;34(3):1339–61. Regio decreto legge 23 ottobre 1924 n. 2089. 1924, Italian Legislation.
- [16] Smoljanovic H, Zivaljic N, Nikolic Z, Munjiza A. Numerical model for confined masonry structures based on finite discrete element method. *Int J Eng Model* 2017;30(1–4):19–35, cited By 14.
- [17] Amouzadeh Tabrizi M, Soltani M. In-plane response of unreinforced masonry walls confined by reinforced concrete tie-columns and tie-beams. *Adv Struct Eng* 2017;20(11):1632–43. <http://dx.doi.org/10.1177/1369433216689569>, cited By 7.
- [18] Borah B, Kaushik H, Singhal V. Lateral load-deformation models for seismic analysis and performance-based design of confined masonry walls. *J Build Eng* 2022;48. <http://dx.doi.org/10.1016/j.jobbe.2021.103978>, cited By 8.
- [19] Yacila J, Camata G, Salsavilca J, Tarque N. Pushover analysis of confined masonry walls using a 3D macro-modelling approach. *Eng Struct* 2019;201. <http://dx.doi.org/10.1016/j.engstruct.2019.109731>, cited By 24.
- [20] Okail H, Abdelrahman A, Abdelkhalik A, Metwaly M. Experimental and analytical investigation of the lateral load response of confined masonry walls. *HBRC J* 2016;12(1):33–46. <http://dx.doi.org/10.1016/j.hbrj.2014.09.004>, cited By 38.
- [21] Janaraj T, Dhanasekar M. Finite element analysis of the in-plane shear behaviour of masonry panels confined with reinforced grouted cores. *Constr Build Mater* 2014;65:495–506. <http://dx.doi.org/10.1016/j.conbuildmat.2014.04.133>.
- [22] Medeiros P, Vasconcelos G, Lourenço P, Gouveia J. Numerical modelling of non-confined and confined masonry walls. *Constr Build Mater* 2013;41:968–76. <http://dx.doi.org/10.1016/j.conbuildmat.2012.07.013>, cited By 57.
- [23] Tarque N, Salsavilca J, Yacila J, Camata G. Multi-criteria analysis of five reinforcement options for Peruvian confined masonry walls. *Earthq Struct* 2019;17(2):205–19.
- [24] Borah B, Kaushik HB, Singhal V. Analysis and design of confined masonry structures: Review and future research directions. *Buildings* 2023;13(5):1282.
- [25] Gupta A, Singhal V. Strengthening of confined masonry structures for in-plane loads: a review. In: *IOP conference series: materials science and engineering*. vol. 936, IOP Publishing; 2020, 012031.
- [26] Vestroni F, Beolchini G, Antonacci E, Modena C. Identification of dynamic characteristics of masonry buildings from forced vibration tests. In: *Proceedings of the 11th world conference on earthquake engineering*. 1996, cited By 10.
- [27] De Sortis A, Antonacci E, Vestroni F. Dynamic identification of a masonry building using forced vibration tests. *Eng Struct* 2005;27(2):155–65. <http://dx.doi.org/10.1016/j.engstruct.2004.08.012>.

- [29] Turek M, Thibert K, Ventura C, Kuan S. Ambient vibration testing of three unreinforced brick masonry buildings in Vancouver, Canada. 2006, cited By 5.
- [30] Nema H, Basu D. Natural properties of confined masonry buildings – Experimental case studies and possible inferences. *Int J Mason Res Innov* 2019;4(3):197–226. <http://dx.doi.org/10.1504/IJMRL.2019.100567>.
- [31] Chakra-Varthy P, Basu D. Natural period and vertical distribution of base shear in confined masonry buildings using ambient vibration test. *Bull Earthq Eng* 2021;19:1851–99.
- [32] Magrinelli E, Acito M, Bocciarelli M. Numerical insight on the interaction effects of a confined masonry tower. *Eng Struct* 2021;237:112195.
- [33] Kumar S, Akbar MA, Thakur A. Seismic analysis of a G+ 3 confined masonry building with AAC infill using SAP 2000. *Mater Today: Proc* 2023;74:718–25.
- [34] Rosso MM, Aloisio A, Parol J, Marano GC, Quaranta G. Intelligent automatic operational modal analysis. *Mech Syst Signal Process* 2023;201:110669.
- [35] DM17/01/2018. Italian standard regulation “norme tecniche per le costruzioni”. Rome, Italy: Italian Ministry of Infrastructures and Transportation; 2018, in Italian.
- [36] Reynders E, Houbrechts J, De Roeck G. Fully automated (operational) modal analysis. *Mech Syst Signal Process* 2012;29:228–50. <http://dx.doi.org/10.1016/j.ymssp.2012.01.007>, URL <https://www.sciencedirect.com/science/article/pii/S0888327012000088>.
- [37] Civera M, Mugnaini V, Zanutti Fragonara L. Machine learning-based automatic operational modal analysis: A structural health monitoring application to masonry arch bridges. *Struct Control Health Monit* 2022;29(10):e3028. <http://dx.doi.org/10.1002/stc.3028>.
- [38] Mugnaini V, Zanutti Fragonara L, Civera M. A machine learning approach for automatic operational modal analysis. *Mech Syst Signal Process* 2022;170:108813. <http://dx.doi.org/10.1016/j.ymssp.2022.108813>.
- [39] Rainieri C, Fabbrocino G. Operational modal analysis of civil engineering structures. vol. 142, New York: Springer; 2014, p. 143.
- [40] Civera M, Pecorelli ML, Ceravolo R, Surace C, Zanutti Fragonara L. A multi-objective genetic algorithm strategy for robust optimal sensor placement. *Comput-Aided Civ Infrastruct Eng* 2021;36(9):1185–202. <http://dx.doi.org/10.1111/mice.12646>, arXiv:<https://onlinelibrary.wiley.com/doi/pdf/10.1111/mice.12646>, URL <https://onlinelibrary.wiley.com/doi/abs/10.1111/mice.12646>.
- [41] Reynolds T, Harris R, Chang W-S, Bregulla J, Bawcombe J. Ambient vibration tests of a cross-laminated timber building. *Proc Inst Civ Eng-Constr Mater* 2015;168(3):121–31.
- [42] Peeters B, De Roeck G. Reference-based stochastic subspace identification for output-only modal analysis. *Mech Syst Signal Process* 1999;13(6):855–78.
- [43] Pasca DP, Aloisio A, Rosso MM, Sotiropoulos S. PyOMA and PyOMA_GUI: A python module and software for operational modal analysis. *SoftwareX* 2022;20:101216.
- [44] Zhou K, Li Q-S. Modal identification of high-rise buildings under earthquake excitations via an improved subspace methodology. *J Build Eng* 2022;52:104373.
- [45] Zhou K, Li Q-S, Han X-L. Modal identification of civil structures via stochastic subspace algorithm with Monte Carlo-based stabilization diagram. *J Struct Eng* 2022;148(6):04022066.
- [46] Gramacki A. Nonparametric kernel density estimation and its computational aspects, vol. 37, Springer; 2018.
- [47] Owen AB. A randomized Halton algorithm in R. 2017, arXiv preprint arXiv:1706.02808.
- [48] Hou T, Nuyens D, Roels S, Janssen H. Quasi-Monte Carlo based uncertainty analysis: Sampling efficiency and error estimation in engineering applications. *Reliab Eng Syst Saf* 2019;191:106549.
- [49] Chatzi EN, Spiridonakos MD, Smyth AW. Implementation of parametric methods for the treatment of uncertainties in online identification. In: *Identification methods for structural health monitoring*. Springer; 2016, p. 51–87.
- [50] Rainieri C, Fabbrocino G. Influence of model order and number of block rows on accuracy and precision of modal parameter estimates in stochastic subspace identification. *Int J Lifecycle Perform Eng* 2014;1(4):317–34, cited By 34.
- [51] Zini G, Betti M, Bartoli G. A quality-based automated procedure for operational modal analysis. *Mech Syst Signal Process* 2022;164:108173.
- [52] Silverman BW. *Density estimation for statistics and data analysis*. Routledge; 2018.
- [53] Bishop CM, Nasrabadi NM. *Pattern recognition and machine learning*, vol. 4, Springer; 2006.
- [54] Wand MP, Jones MC. *Kernel smoothing*. CRC Press; 1994.
- [55] Botev ZI, Grotowski JF, Kroese DP. *Kernel density estimation via diffusion*. 2010.
- [56] Ordinanza del Presidente del Consiglio dei Ministri del 20 Marzo 2003. *Primi elementi in materia di criteri generali per la classificazione sismica del territorio nazionale e di normative tecniche per le costruzioni in zona sismica*. 2003, Gazzetta Ufficiale (G.U.).
- [57] Goldberg D. *Genetic algorithms in search, optimization and machine learning*, addition-westly. Reading MA; 1989.
- [58] Coello CAC. Theoretical and numerical constraint-handling techniques used with evolutionary algorithms: a survey of the state of the art. *Comput Methods Appl Mech Engrg* 2002;191(11–12):1245–87.
- [59] Michalewicz Z, Schoenauer M. Evolutionary algorithms for constrained parameter optimization problems. *Evol Comput* 1996;4(1):1–32.